The application of SIMS ion imaging techniques in the experimental study of fluid–mineral interactions

S. C. Elphick, C. M. Graham, F. D. L. Walker and M. B. Holness

Department of Geology and Geophysics, University of Edinburgh, West Mains Road, Edinburgh EH9 3JW

Abstract

Ion imaging by SIMS (ion microprobe) techniques provides a novel approach to the identification of mechanisms of fluid–mineral interaction during hydrothermal experiments. In scanning ion imaging, the primary ion beam is focussed to a fine spot which is rastered across the polished sample surface, and the secondary ion signal from the mass spectrometer is synchronised with the primary beam. The resistive anode encoder provides a direct ion image of a sample surface illuminated by a defocussed primary beam. The latter system is susceptible to charging artifacts during the imaging of insulating geological materials, and has a lower dynamic range than the scanning ion imaging system.

Application of both systems to the study of fluid–mineral interaction during hydrothermal experiments are reviewed in which fluid or solid phases have been labelled with ^{18}O-enriched isotopic tracers. These include studies of micropermeability and microporosity in feldspars, solid-state diffusion versus solution-reprecipitation, textural equilibration mechanisms, and oxygen isotope exchange in silicate–carbonate systems.

Keywords: ion microprobe, ion imaging, fluid-mineral interaction, isotope tracers, solution-reprecipitation, oxygen exchange.

Introduction—the ion microprobe

Secondary Ion Mass Spectometry (SIMS, Ion Microprobe) is an analytical technique which has significantly enhanced the analytical capabilities available in the Earth Sciences. SIMS has three important assets: high spatial resolution, great elemental sensitivity, and the ability to separate isotopes. In this article we will be considering some of the ion imaging capabilities of modern SIMS, with particular reference to the Cameca ims-4f ion microprobe/microscope instrument, as installed at the Department of Geology and Geophysics, University of Edinburgh.

The general principles of the SIMS method are reviewed in detail by Slodzian (1980), and geological applications of SIMS by Reed (1989). Ionising sources (ion guns) supply a high-energy, positively or negatively charged primary beam of atoms (commonly Cs^+ or O^-) to the *primary* column, along which they are focussed onto the sample where they slowly ablate part of the sample surface. Charged species sputtered by this primary beam are electrostatically extracted via the *secondary* column to a mass spectrometer. There the desired sputtered species is separated by mass and energy, before impinging on either a viewing plate or counting system.

Secondary ion yields are dependent on the primary beam species. Oxygen, including both that originally in the sample and that added from the primary beam, enhances the generation of positive secondary ions because of its affinity for electrons. Electropositive primary ions such as Cs^+ enhance the secondary ionisation of electronegative elements, such as oxygen or sulphur.

The apparatus is maintained at high vacuum, with the sample introduced through an airlock. Samples, which must be vacuum-compatible, can be flat polished sections, grains mounted and polished in epoxy blocks, or crystals embedded in metal foil. A typical working minimum primary beam spot size, using Cs^+ or O^- is ~0.5 to 5μm diameter.

Principles of ion imaging

Scanning Ion Imaging (SII)

There are two different methods of forming an ion image of the sample surface in the Cameca

Mineralogical Magazine, September 1991, Vol. 55, pp. 347–356

ims-4f. In *Scanning Ion Image* (SII) configuration, the primary beam is focussed to a fine spot, which is rastered (scanned) across the sample by electrostatic deflectors in the primary column. By synchronisation of the secondary ion signal from the mass spectrometer with primary beam position, an ion image of an area up to 500μm^2 of the sample surface can be produced (Fig. 1*a*).

The SII system has a large dynamic range (i.e. both high and low count rates may be detected). The resolution of the SII is beam-size dependent. High count rates on elements present at low abundances are gained at the expense of sharpness of the final image, because higher primary beam currents are achieved at the expense of larger beam spot sizes. To minimise beam spot sizes, SII typically uses pico-amp beam currents, giving ~2μm resolution in the image.

Resistive Anode Encoder (RAE)

Alternatively, the Cameca ims-4f is capable of providing a direct ion image of the sample surface. In this mode, a broad area of the sample is illuminated by the defocussed or rastered primary ion beam (Fig. 1*b*). The resulting sputtered species pass through the mass spectometer via the secondary ion optics, which have been designed to maintain the original relative spatial relationships at the sample suface. Thus an imaging plate placed at the correct focal position after the mass spectrometer will record a real, magnified ion image of the sample surface, which may be recorded by photographic methods, CCD cameras, or a *Resistive Anode Encoder* (RAE) system.

The Cameca ims-4f at the Department of Geology and Geophysics, University of Edinburgh, is equipped with the Charles Evans and Associates' RAE system for the recording and digitising of the ion image. In this system, secondary ions strike a set of multichannel plates (Fig. 2). These plates convert the incoming ion into a pulse of electrons, which impact a resistive plate. The position of this impact may be calculated by measuring the charge at four electrodes oriented at 90° to each other. Over a period of time, the cumulative ion arrivals at the RAE plane build up an ion image of the sample surface. A more detailed account of the Charles Evans and Associates RAE system is given by Odom *et al.* (1983), and the principles of microchannel plate detectors are described by Wiza (1979).

In RAE mode, image resolution is limited by the resolution of the secondary ion optics and image detection system. Thus, resolution is not dependent on primary beam current density, because the beam is only being used to illuminate the surface. RAE imaging is also limited by its low dynamic range, because low count rates are required to prolong the lifetime of the channel plates and resistive elements, and also because the system has large dead-times (typically about 3μs) in the positioning electronics.

Sample charging and imaging artifacts

In SIMS studies of geological materials, which are usually insulators, imaging is complicated by the necessity of avoiding charging of the sample, which is related to the type of primary beam used. Generally, positive secondary ions such as Si^+ or Nb^+ are sputtered using a negative (i.e. O^-) primary beam, which leads to a build-up of negative charge on the sample. If negative secondaries such at S^- or O^- are required, a positive primary beam such as Cs^+ is normally used, leading to positive charging of insulating samples. To mitigate charging problems encountered in non-conducting samples, and to provide a uniform electrostatic extraction field, SIMS samples are generally vacuum sputter-coated with gold.

For negative primary beams, electron loss over the sample surface normally prevents excessive charging. However, for a positive primary beam there is substantial positive charging, which requires charge neutralisation. In the Cameca system, this is accomplished using a broad-area, low-energy electron flood gun aimed through the secondary column and normal to the sample surface. In both positive and negative modes, residual charge build-up may result in image artifacts, which are discussed in more detail below.

Because the gold coating required for charge equilibration is microporous, one can obtain an ion image of the substrate through the sputter coating, although with greatly reduced count rates. As the coating is ablated by the primary beam, the image will brighten until the conductivity of the sample surface deteriorates. The image then tends to flicker or move slightly as a new electrostatic balance is achieved at the surface, and any further imaging will be prone to charging artifacts and image degradation. The best images are obtained when the gold coating has been thinned, but is still intact.

For insulators, the image quality is often limited by artifacts of charge neutralisation. At high primary beam currents, the image is distorted by surface electrostatic inhomogeneities arising from the interaction between the primary

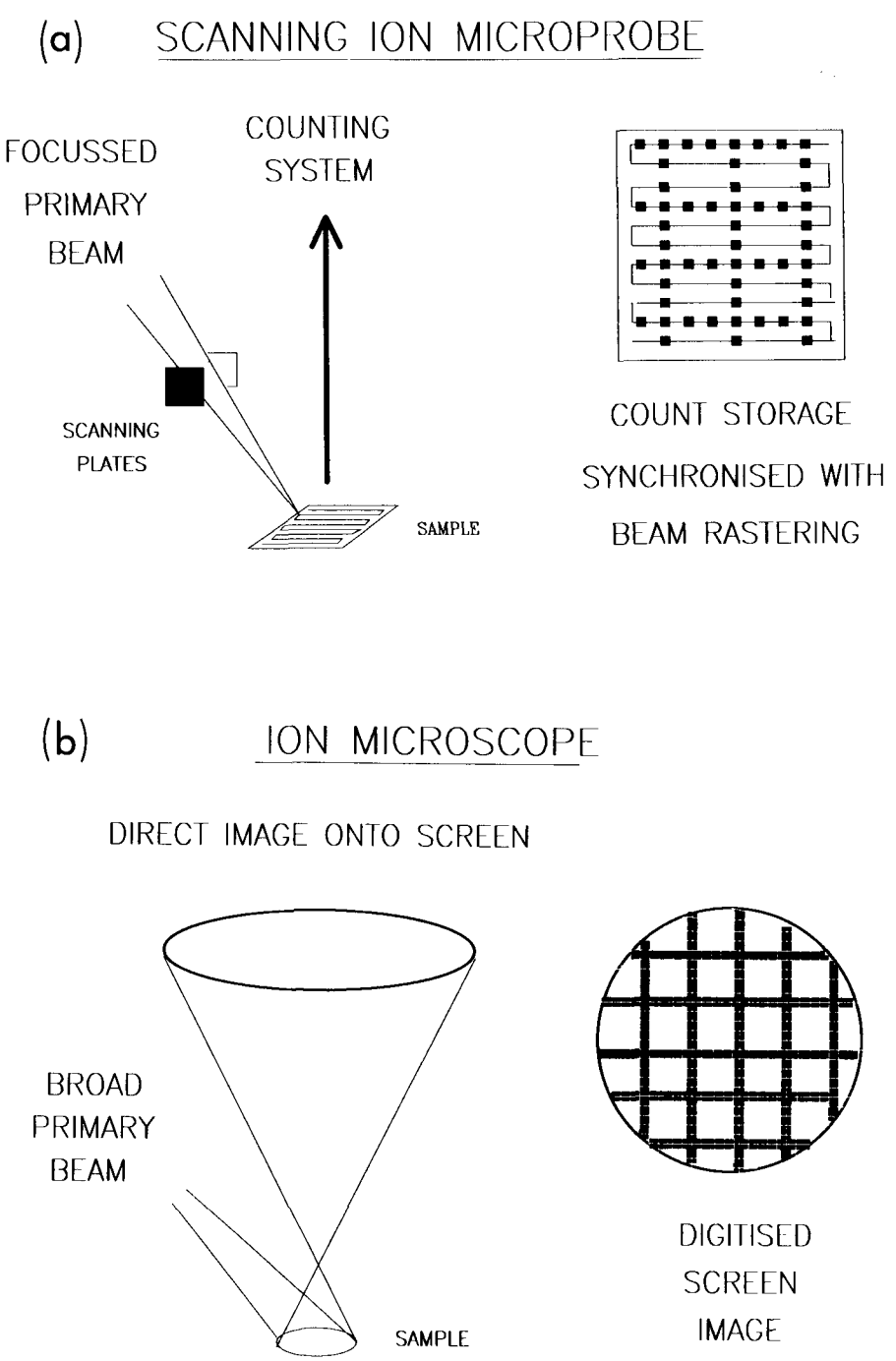

FIG. 1. Illustrations of the principles of operation of: (*a*) the Scanning Ion Image system of the Cameca ims-4f ion microprobe with Charles Evans and Associates control and imaging systems, as configured at the Ion Microprobe Facility at the University of Edinburgh; (*b*) the Resistive Anode Encoder (RAE) system.

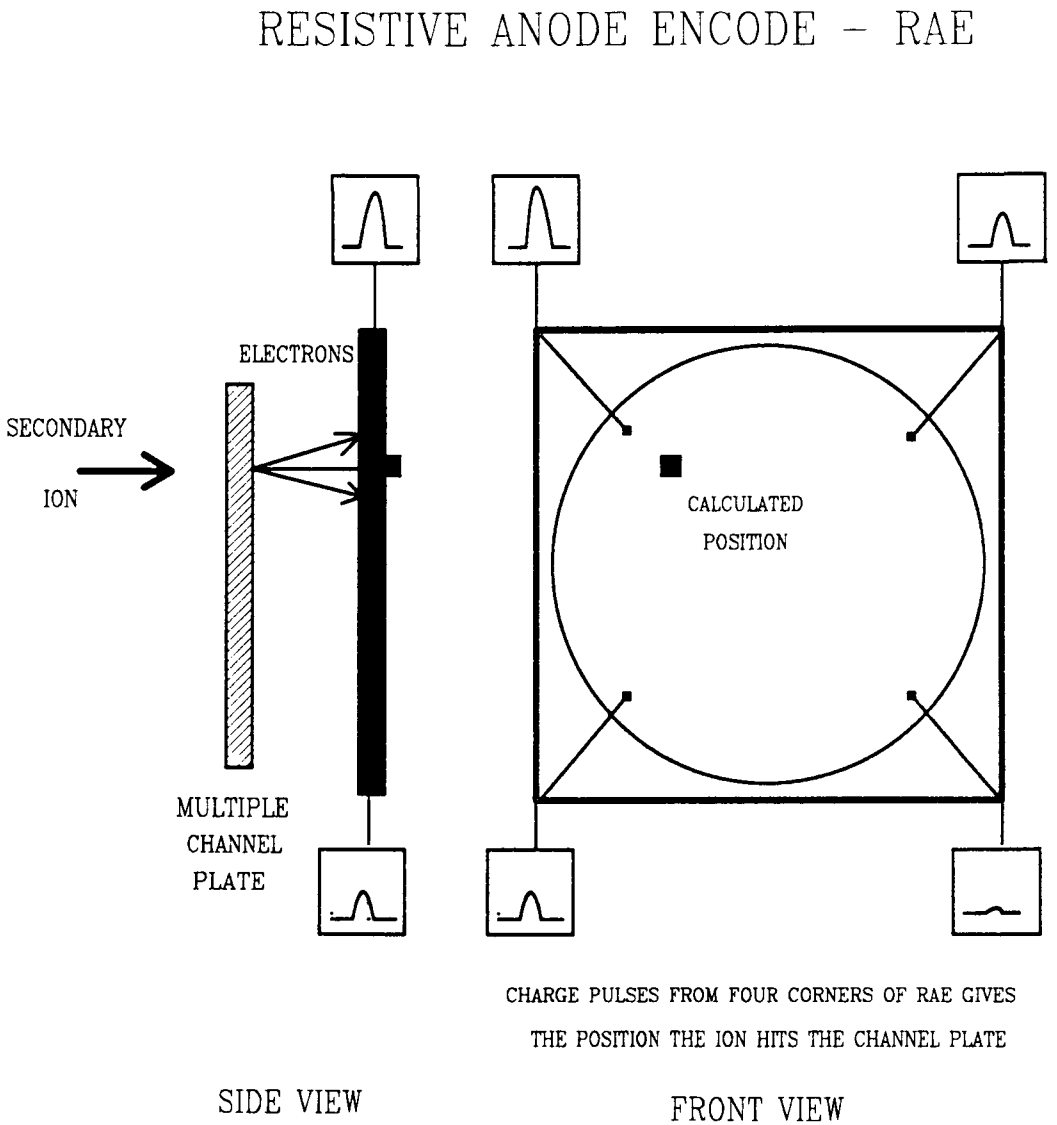

FIG. 2. Illustration of the principle of operation of the Charles Evans and Associates Resistive Anode Encoder system, showing the conversion of the secondary ion signal into an electron pulse at the resistive plates, on which the spatial location of the impacting secondary ions is recorded. See text for discussion.

beam, the electron flood gun, and near-surface electron movement. The result is similar to optical imaging through non-uniformly heated air, with the same shimmer in the image.

Another complication which can cause imaging problems is the angle of impingement of the primary beam on the sample surface. For the Cameca system, the primary beam strikes at ~30° from the sample normal. With an inclined beam, topographic artifacts may arise on images (see Plate 2*b*).

As in any other measurement technique, the images obtained from SIMS require careful analysis. It is important to note that the image finally obtained is a record of sample surface secondary ion intensity, rather than absolute concentrations of imaged species. Thus an image of a perfectly homogeneous insulating substrate can still give an inhomogeneous image due to spatial variation of residual charge, or relief features of the surface. However, many problems can be minimised by image processing. For

example, ^{18}O and ^{16}O images of an isotopically zoned crystal will display identical artifacts. Therefore pixel by pixel division of the two images to give a combined $^{18}O/^{16}O$ image will eliminate most image artifacts, except those arising from counting statistics. Thus combining images can give improved information on the spatial distribution of the isotopes.

Conclusions

In both the SII and RAE imaging systems, resolution is gained at the expense of count rates, and there is a trade-off between image quality and secondary ion sensitivity. Resolutions on the two systems are comparable, but image acquisition is somewhat faster on the direct imaging RAE system relative to the SII. However, the SII is less susceptible than the RAE to charging artifacts, because a smaller beam (typically pico-amps) is rastered over the imaged area. On balance, the lower dynamic range and higher backgrounds of the RAE system relative to the SII result in the SII being more widely used.

Although the difficulties of SIMS imaging for geological samples have been explored, it cannot be too strongly emphasised that it is an extremely powerful technique. Using SIMS, one can examine the spatial distribution of isotopes present in very low concentrations, and also relative isotopic concentrations. No other technique can yield the wealth of detail which can be explored through SIMS imaging.

Applications to experimental mineralogical, textural and fluid–mineral interaction studies

This section is devoted to the use of SIMS imaging in experimental studies. Here it is particularly useful because the experimentalist has some control of the isotopic composition of working fluids and solids. For example, in the simplest cases, by using $H_2{}^{18}O$ in charges, any solid which has undergone a solution-reprecipitation step can be selectively imaged through the ^{18}O signature it acquired from the fluid phase. Examples of this technique are documented below.

Micropermeability in alkali feldspars

Scanning ion imaging (SII) of ^{18}O tracer in hydrothermal experiments has provided a powerful tool for the mapping of microporosity and micropermeability in alkali feldspars (Walker, 1990). Turbidity in feldspars is the result of micron to sub-micron scale micropores, as demonstrated by recent work using TEM and SEM techniques (Finch and Walker, 1991; Worden *et al.*, 1990, inter alia). The presence of micropores may have profound effects on the chemical reactivity, diffusion properties and physical behaviour of feldspars. For example weathering and diagenetic behaviour, effective grain sizes for diffusion, retentivity of argon (Parsons *et al.*, 1988), and rates and mechanisms of fluid-mineral interaction and oxygen isotope exchange may all depend on micropore density.

The connectivity and hence permeability of the micropores is a critical factor in the process detailed above. This connectivity can be studied experimentally at high P and T using $H_2{}^{18}O$ tracers, followed by SII. Alkali feldspar cleavage fragments of various size ranges (200–220μm, 1–2 mm) were heated at 700°C, 1 kbar, in sealed gold capsules containing 30% by weight of 99% $H_2{}^{18}O$, for periods of from 75 to 1700 hours. Fragments were then mounted and polished to expose grain sections, and imaged for ^{18}O using the scanning ion image system. Images were matched against SEM images of the micropores of the same grains. An unexchanged fragment of feldspar was also imaged for reference.

Connectivity of micropores would be demonstrated if enrichment of ^{18}O occurred in the centres of grains, around pores identified in matching SEM pictures, and away from cracks and grain boundaries. In the absence of micropore connectivity, ^{18}O enrichment would be restricted to grain edges and cracks, being limited by the volume diffusion of oxygen in feldspar (Elphick *et al.*, 1988). Plate 2*a* shows the ^{18}O distribution across a grain of exchanged feldspar, demonstrating that ^{18}O has penetrated into microporous areas in the centre of the grain. ^{18}O enrichment is also evident along cracks (which must therefore have been open during annealing and exchange) and grain edges, the latter due to inward volume diffusion of oxygen, probably accompanied by some solution-reprecipitation. This simple and powerful application of scanning ion imaging has confirmed the connectivity of micropores in alkali feldspar grains, with the important geological implication that the effective dimension for diffusion during feldspar–fluid exchange in the Earth's crust may be reduced by orders of magnitude relative to the observed crystal size.

Mineral–fluid exchange mechanisms: diffusion versus solution-reprecipitation

Central to the interpretation of data from any experimental diffusion study is the demonstration

that the process being measured is the solid-state process of volume diffusion rather than surface reaction and solution-reprecipitation. In many diffusion studies involving the bulk analysis of the mineral and/or the fluid (including supercritical aqueous fluid and gas) after a mineral–fluid exchange experiment at high temperature, the extent of reaction or exchange is treated as a volume diffusion process in order to calculate diffusivities. However, much or all of the 'diffusion' process might be attributable to surface reaction/dissolution processes. Examples include oxygen isotope exchange experiments, oxygen and hydrogen diffusion studies, and Al–Si order–disorder studies such as those detailed in Elphick *et al.* (1986) and Graham and Elphick (1990*a,b*).

Scanning ion imaging of tracers such as ^{18}O in experimental run-products following mineral–fluid exchange experiments leads to quantification of the extent of solution-reprecipitation versus solid-state diffusion, and thus allows testing of the validity of modelling the extent of exchange or order–disorder as a volume diffusion process.

Diffusion-dominated systems: Al–Si disordering in albite. We illustrate this application of ion imaging with a study of the mechanism of Al–Si disordering in albite at high pressure and temperature (Graham and Elphick, 1990*a*). The rate of Al–Si disordering of ordered albite in presence of aqueous fluid is significantly enhanced by the presence of dissolved salts, and increases with increasing NaCl molarity of NaCl–H_2O solutions. This rate enhancement has been attributed to the activity of H^+ in solution, which in turn increases the concentration of H^+ on the lattice. In order to establish that this rate enhancement is due to mediation of H^+ in the solid-state Al–Si interdiffusion mechanism rather than dissolution–reprecipitation, experiments have been run with sized grains of Amelia albite and $H_2{}^{18}O$ with excess NaCl in sealed Pt capsules at 850°C and 1 and 17 kbars. Under these conditions, X-ray study shows that complete Al–Si disorder is attained.

The resulting scanning ion image of typical ^{18}O distribution in the albite grains is shown in Plate 2*b*. Areas of original, unrecrystallised albite show low ^{18}O content. However, material which has dissolved and reprecipitated as new albite has acquired a large ^{18}O content derived from the fluid, and forms broad zones and overgrowths on the original albite core. All crystals show a thin rim of ^{18}O derived from volume diffusion of oxygen inwards from the crystal–fluid interface, as expected from Elphick *et al.* (1986). The left and right edges of the albite crystal in Plate 2*b* differ significantly in brightness. This is an image artifact arising from the combination of inclined primary beam geometry and polish rounding of the crystal surface.

The scanning ion imaging system software permits line scans of pixel counts versus distance to be constructed. Thus in Fig. 1*c* we see an ^{18}O concentration profile across a crystal showing two wide zones of overgrowth. This profile demonstrates the sharp drop in ^{18}O signal at the outer edge of the crystal, in contrast to the S-shaped interdiffusion profile between the original ^{16}O-rich crystal core and the ^{18}O-rich overgrowth. From this latter part of the profile it is possible to estimate the diffusivity of oxygen in albite at the experimental conditions, and to show that this diffusivity is in good agreement with that more accurately derived from depth-profile analysis (Elphick *et al.*, 1986). With these ^{18}O labelling techniques we have been able to show that Al-Si interdiffusion and disordering has proceeded dominantly by solid-state mechanisms during annealing of albite in saline solutions at 1 and 17 kbars even although variable amounts of solution-reprecipitation have occurred.

Solution-reprecipitation dominated systems: $KGaSi_3O_8$. An extreme example of solution-reprecipitation is illustrated in Plate 2*d*. Coarsely crystalline gallium sanidine ($KGaSi_3O_8$) was synthesized hydrothermally from glass fragments at 800°C and 1 kbar for 5 days, yielding large elongate crystals over 100μm wide and hundreds of microns in length. A sample of this sanidine was re-annealed at 400°C and 1 kbar with $H_2{}^{18}O$-labelled 2M KOH solution for 40 days, and the resulting KGa-microcline run product [kindly synthesized and supplied by J. Göttlicher and H. Kroll (Münster)] imaged for ^{18}O and ^{16}O. Only one crystal of dominantly ^{18}O-free feldspar starting material was found in the imaged portion of the run product, and this is shown in Plate 2*d*. This crystal is rimmed by ^{18}O-rich feldspar, and has a history similar to the albite in Plate 2*b*. Alongside this crystal is an array of grains of varying size which are all variably enriched in ^{18}O. The large crystal in the upper part of the plate is in fact enriched in ^{18}O in the core relative to the rim.

This pattern of variable ^{18}O concentrations reveals a complex growth history in the re-annealed sample. The rarity of ^{18}O-poor feldspar cores demonstrates that almost complete solution of KGa sanidine and reprecipitation of KGa microcline has occurred. As this process proceeded, early crystals formed with the high ^{18}O signature of the early fluid, but this fluid was then continuously diluted with ^{16}O from the dissolving feldspar, and so later crystals grew with progress-

ively lower ^{18}O contents. Thus,the $^{18}O/^{16}O$ ratio in a crystal shows its relative age in the solution-reprecipitation cycle. In a complex sample such as this, the crystal distribution can be easily mapped by imaging for ^{35}Cl, which reveals distribution of araldite mounting compound between the grains.

Oxygen isotope exchange in silicate–carbonate systems

There has been considerable recent interest in the recalibration of oxygen isotope fractionation factors amongst silicate and oxide minerals at high pressures and temperatures, using calcite as a common exchange medium (Chiba et al., 1989; Clayton *et al.*, 1989). In these experiments, conducted in a solid media apparatus using NaCl pressure cells, oxygen exchange between silicates and calcite in the absence of water was at reaction rates comparable to those of oxygen isotope exchange between silicates and water, with fewer experimental complications.

To illustrate the use of SIMS imaging in addressing the question of the mechanism of this rapid exchange process, a similar exchange experiment has been conducted using albite powder of 50–250μm grain-size and ^{18}O-labelled $CaCO_3$ sealed in a Pt capsule. The experiment was performed at 17 kbars, 700°C for 52 hours in a piston cylinder apparatus, using an NaCl pressure cell. At the end of the experiment, the albite was acid-washed with dilute HCl to remove the calcite, and mounted in epoxy before polishing to section the grains.

Plate 3*a, b,* and *c* are of RAE images of a polished section through the centre of an albite grain, and illustrate some of the subtleties of interpretation required in experimental studies. Only albite and $CaC^{18}O_3$ were included in the original charge, and hydrogen may or may not have diffused through the capsule wall during the anneal. The grain-size of the carbonate both before and after the run was submicron, so that even in the absence of any intergranular melt or fluid, grain-boundary diffusion of ^{18}O through the calcite would ensure homogeneity of ^{18}O content. Hence any calcite imaged must show strong signals for both ^{40}Ca and ^{18}O. Any Ca feldspar formed by solution-reprecipitation will also show high ^{40}Ca and ^{18}O.

Plate 3*a* shows the distribution of mass 18 in the section. Both the edges and a long fracture in the grain show high counts, with the image also showing a slight shadowing artifact through lower counts along the bottom edge of the grain. The complementary mass 40 image (Plate 3*b*) shows high counts around the grain edge, but not at the grain centre. Thus the bright fracture in Plate 3*a,* missing in Plate 3*b,* cannot represent trapped $CaC^{18}O_3$ in the crystal core. This bright feature is therefore interpreted to be a crack in the crystal, present during the experiment, along which ^{18}O has moved and diffused into the fracture walls. We thus see both grain boundary and volume diffusion processes at work.

Plate 3*b* shows that the mass 40 signal is restricted to the albite edge, although there was a fracture open to oxygen movement during the experiment. If the rim of the grain reacted with $CaCO_3$ to form a calcic phase, so too should the fracture edge, which would give a bright crack feature in the mass 40 image. We can thus deduce that the mass 40 material at the grain edge was not derived from the experiment by reaction or diffusion. We have already noted that mass 40 and mass 18 images must be correlated in any image of $CaC^{18}O_3$ remaining from the experimental charge. Comparison of the two grain edge images 3*a* and 3*b* shows this criterion is not met, so we can be sure that the mass 40 signal does not arise from the experiment. Thus the mass 40 material along the edge in Plate 3*b* must be post-experimental contamination of the grain edge, during the later mounting or polishing steps.

The interpretation of the mass 18 and 40 images can be confirmed by examining other mass images. Thus Plate 3*c*, a mass 24 image, again shows a signal confined to the main edge. Since no ^{24}Mg was present in the orignal experiment, we can be sure that this image arises from post-experimental processes, such as mounting or polishing problems, confirming the interpretation of Plate 3*a* and *b*.

The ion image study of this experimental charge demonstrates that there had been no trapping of $CaC^{18}O_3$ in albite grains during the high pressure anneal, which would drastically affect the interpretation of measured oxygen fractionation factors. The ^{18}O image shows clearly that oxygen from $CaC^{18}O_3$ has exchanged along fractures present at high pressure, as well as by diffusion across grain boundaries. The scale of ^{18}O exchange is so limited, however, that it is evident that exchange has not been enhanced by high pressure.

Textural equilibration in marbles

A critical but poorly constrained control on fluid transport in rocks at depth in the Earth's crust is the geometry of fluid-filled porosity, which will determine the partitioning of fluid flow between microcracks and stable, interconnected grain-edge porosity during metamorphism and related

devolatilisation reactions. The permeability–porosity relationships for stable grain-edge porosity in solid–fluid systems are dependent on the fluid–solid dihedral angle, if the fluid is in textural equilibrium with the solid (e.g. Von Bargen and Waff, 1986; Watson and Brenan, 1987). Rates of fluid–solid textural equilibration in forsterite marbles have been experimentally investigated at high P and T by monitoring the change of forsterite–calcite–calcite dihedral angle with time in the approach to the equilibrium dihedral angle (Holness *et al.*, 1990).

The mechanisms of the grain-shape modifying processes, which lead to textural equilibration during the experiments, may be followed using an appropriate isotopic tracer in the fluid or solid. In the typical example discussed here, an H_2O–CO_2 fluid labelled with $H_2{}^{18}O$ and a mixture of ground calcite spar and natural forsterite was annealed with 5 wt.% of a fluid of $X(CO_2) = 0.5$ at 1 kbar and 650°C for varying times. Scanning ion images were collected for masses 16 (^{16}O), 18 (^{18}O), 28 (^{28}Si) and 24 ($^{12}C_2$), the latter mass image defining the cracks and pore space in the sample due to the much larger ion yield from the epoxy and diamond paste relative to carbonate.

The distribution of ^{18}O in a sample annealed for only 15 minutes is shown in Plate 3*d*. Fig. 3 shows a replot of the ^{18}O information in shades of grey, with the grain boundaries, cracks and pores, and forsterite grains, delineated. This image combines information from optical examination, $^{12}C_2$ and ^{28}Si images. Plate 3*d* shows the strong ^{18}O zonation in large calcite crystals (e.g. cc_1–cc_3,

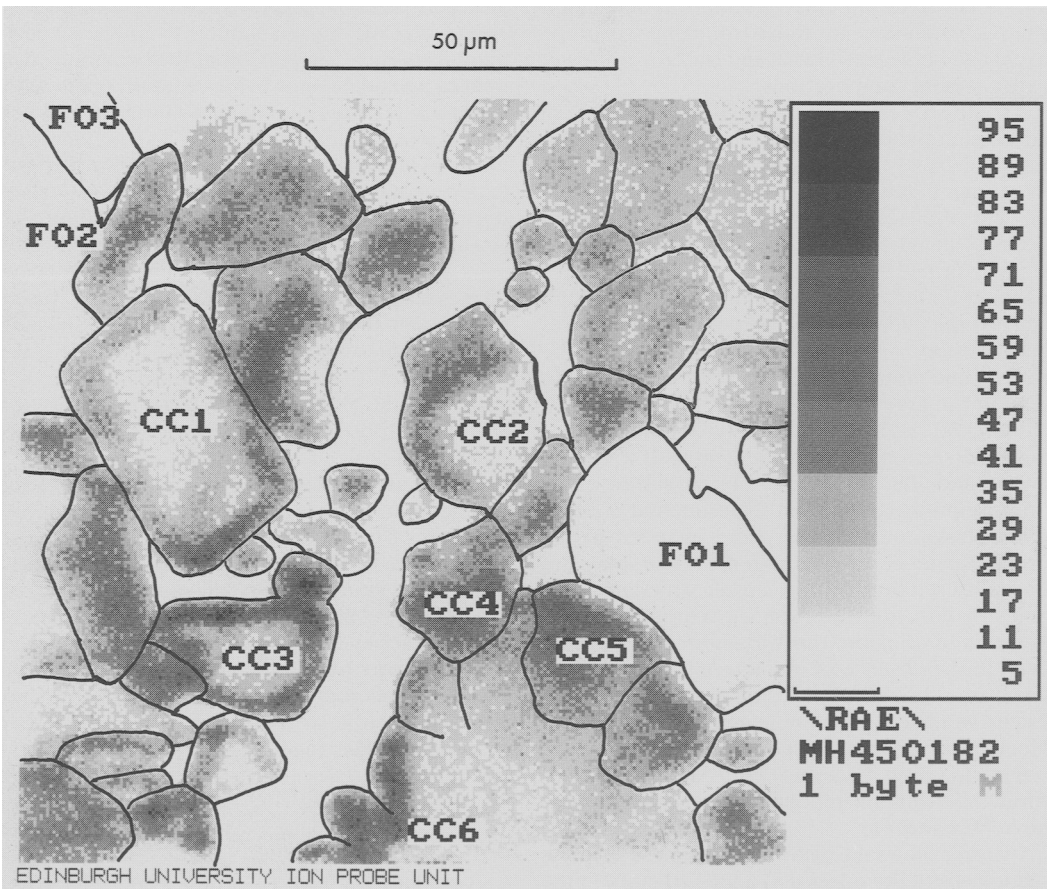

FIG. 3. Scanning ion image of ^{18}O distribution in a calcite (cc)–forsterite (fo) run product annealed at 1 kbar, 650 °C for 15 minutes, with 5 wt.% H_2O–CO_2 fluid ($X(CO_2) = 0.5$) with 14% total oxygen in the fluid present as ^{18}O. Inset bar scale shows ^{18}O counts per pixel, given as a range for each shade of grey (cf. Plate 2*d*). Heavy outlines of the grains are drawn by hand, after comparison of the ion image with the sample thin-section. After Holness *et al.* (1991, in press).

Fig. 3), and the wide ^{18}O-rich rims from precipitation of calcite overgrowths on large fragments of ^{18}O-poor starting material, leading to the development of regular, curvilinear calcite grain boundaries. Other ^{18}O-rich patches not surrounding ^{18}O-poor cores may be attributed to the growth of new interstitial calcite infilling pore spaces and cracks between original calcite fragments (e.g. cc_4–cc_6).

It is noticeable that forsterite grains have low ^{18}O (e.g. fo_1–fo_3), and therefore did not participate in the textural equilibration process to any measurable extent on the short time-scale of this experiment. In longer runs, rapid dilution of the fluid in ^{18}O by ^{16}O from dissolving calcite homogenises the oxygen in the system to the extent that ^{18}O can no longer act as a tracer of the equilibration mechanism. In order to circumvent this limitation in experimental design and to image the movement of forsterite grain boundaries which must inevitably be involved in the subsequent stages and mechanisms of textural equilibration, it will be necessary to use ^{18}O-labelled forsterite.

Summary

In this paper we have discussed the application of ion microprobe imaging techniques to some simple experimental problems involving mineral-fluid interaction. Using only a single tracer such as ^{18}O has yielded a wealth of information not otherwise easily obtainable. Obviously, the use of multiple tracers would enhance the power of the technique still further. The combination of ion microprobe selectivity with modern image analysis provides a new and powerful tool in the earth sciences.

Acknowledgements

We thank Cameca UK Ltd for defraying the cost of publication of the colour plates, and David Polya and Giles Droop for the opportunity to present the applications of these new techniques in the study of mineral textures to a wider audience. Progress on the development and application of the imaging techniques described in this paper would not have been possible without the support of John Craven and Richard Hinton. Jorg Göttlicher and Herbert Kroll (Münster) kindly allowed us to use scanning ion images of their synthetic $KGaSi_3O_8$. The Ion Microprobe Facility at Edinburgh University is supported by NERC. The financial support of British Petroleum and The Industry Department for Scotland in the purchase of the Scanning Ion Imaging System is gratefully acknowledged.

References

Chiba, H., Chacko, T., Goldsmith, J. R., and Clayton, R. N. (1989) Oxygen isotope fractionations involving diopside, forsterite, magnetite and calcite: application to geothermometry. *Geochim. Cosmochim. Acta,* **53**, 2985–95.

Clayton, R. N., Goldsmith, J. R., and Mayeda, T. K. (1989) Oxygen isotope fractionation in quartz, albite, anorthite and calcite. Ibid., **53**, 725–33.

Elphick, S. C., Dennis, P. F., and Graham, C. M. (1986) An experimental study of the diffusion of oxygen in quartz and albite using an overgrowth technique. *Contrib. Mineral. Petrol.*, **92**, 322–30.

—— Graham, C. M., and Dennis, P. F. (1988) An ion microprobe study of anhydrous oxygen diffusion in anorthite: a comparison with hydrothermal data and some geological implications. Ibid., **100**, 490–5.

Finch, A. A. and Walker, F. D. L. (1991) Cathodoluminescence and microporosity in alkali feldspars from the Blå Måne Sø perthosite, South Greenland. *Mineral. Mag.*, in press.

Graham, C. M. and Elphick, S. C. (1990*a*) A re-examination of the role of hydrogen in Al–Si interdiffusion in feldspars. *Contrib. Mineral. Petrol.*, **104**, 481–91.

—— —— (1990*b*) Some experimental constraints on the role of hydrogen in oxygen and hydrogen diffusion and Al–Si interdiffusion in silicates. *Advances in Physical Geochemistry,* **8**, 248–85.

Holness, M. B., Bickle, M. J., and Graham, C. M. (1991) On the kinetics of textural equilibration in forsterite marbles. *Contrib. Mineral. Petrol.*, in press.

Odom, R. W., Furman, B. K., Evans, C. A., Bryson, C. E., Petersen, W. A., Kelly, M. A., and Wayne, D. H. (1983) Quantitative image acquisition system for ion microscopy based on the resistive anode encoder. *Anal. Chem.*, **55**, 574–8.

Parsons, I., Rex, D. C., Guise, P., and Halliday, A. N. (1988) Argon-loss by alkali feldspars. *Geochim. Cosmochim. Acta,* **52**, 1097–112.

Reed, S. J. B. (1989) Ion microprobe analysis–a review of geological applications. *Mineral. Mag.*, **53**, 3–24.

Slodzian, G. (1980) Microanalyzers using secondary ion emission. *Advances in Electronics and Electron Phys.* Supplement, **13B**, 1–43.

Von Bargen, N. and Waff, H. S. (1986) Permeabilities, interfacial areas and curvatures of partially molten systems: results of numerical compositions of equilibrium. *J. Geophys. Res.*, **91**, 9261–76.

Walker, F. D. L. (1990) Ion microprobe study of intragrain micropermeability in alkali feldspar. *Contrib. Mineral. Petrol,* **106**, 124–8.

Watson, E. B. and Brenan J. M. (1987) Fluids in the lithosphere, I. Experimentally determined wetting characteristics of CO_2–H_2O fluids and their implications for fluid transport, host-rock physical properties, and fluid inclusion formation. *Earth Planet. Sci. Letters,* **85**, 497–515.

Wiza, J. L. (1979) Microchannel plate detectors. *Nucl. Instrum. Methods,* **162**, 587–601.

Worden, R. H., Walker, F. D. L., Parsons, I., and Brown, W. L. (1990) Development of microporosity, diffusion channels and deuteric coarsening in perthitic alkali feldspars. *Contrib. Mineral. Petrol.*, **104**, 507–15.

[*Revised manuscript 4 March 1991*]

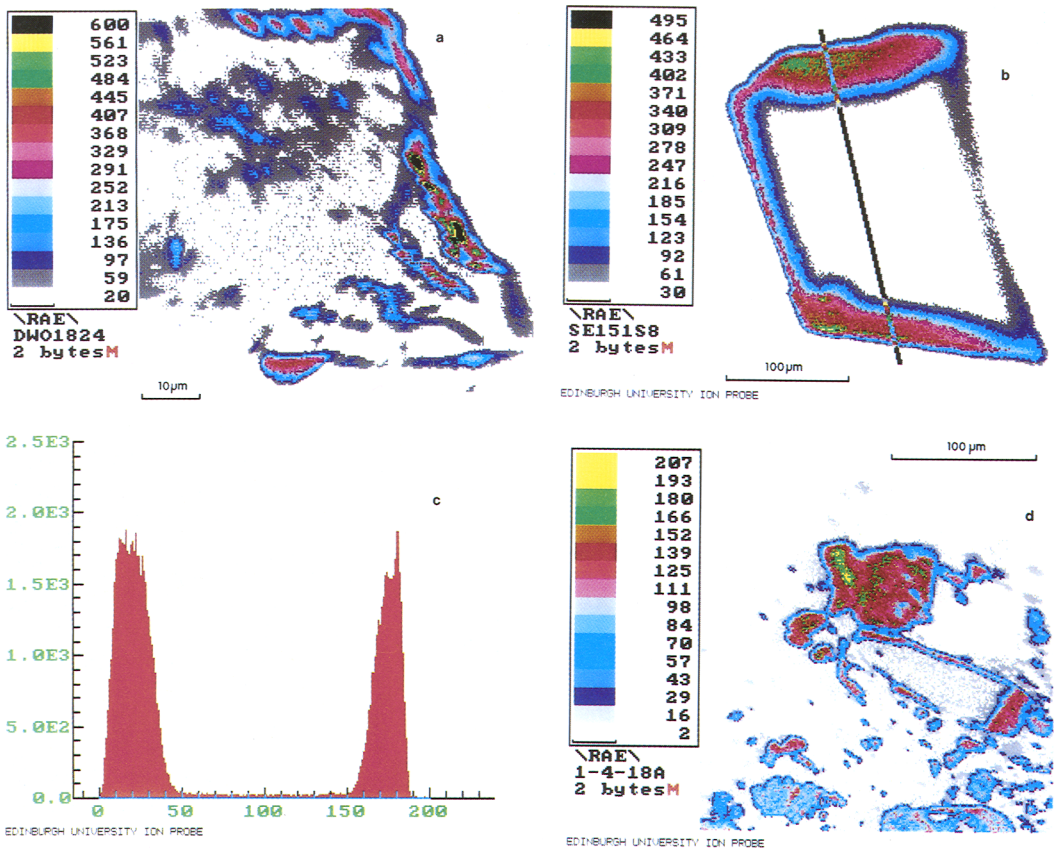

PLATE 2. (*a*) Scanning ion image accumulated over three minutes' counting time of a polished section through a cleavage fragment of alkali feldspar heated in $H_2{}^{18}O$ for 75 hrs, showing the distribution of ^{18}O. The scale bar shows the accumulated counts per pixel. After Walker (1990).

(*b*) Scanning ion image of ^{18}O distribution in Amelia albite heated at 17 kbars and 850 °C in NaCl saturated $H_2{}^{18}O$ (99%) in a salt pressure cell in the piston cylinder apparatus. The scale bar shows the accumulated counts per pixel. Line indicates the position of the line scan in Plate 2(*c*).

(*c*) Line scan across Amelia albite crystal in Plate 2(*b*), showing ^{18}O counts versus distance along a summed 15-pixel width strip. Note sharp outer edges, plateau concentration in the overgrown material, and interdiffusion profile between substrate and overgrowth.

(*d*) Scanning ion image of ^{18}O distribution in crystals of KGa sanidine synthesised hydrothermally at 800 °C and then re-annealed in $H_2{}^{18}O$ at 400 °C and 1 kbar for 40 days (sample kindly supplied by J. Göttlicher and H. Kroll (Münster)). Scale bar shows accumulated counts per pixel. Note relic core of ^{18}O-poor feldspar and high ^{18}O concentrations in centre of feldspar newly grown by solution-reprecipitation.

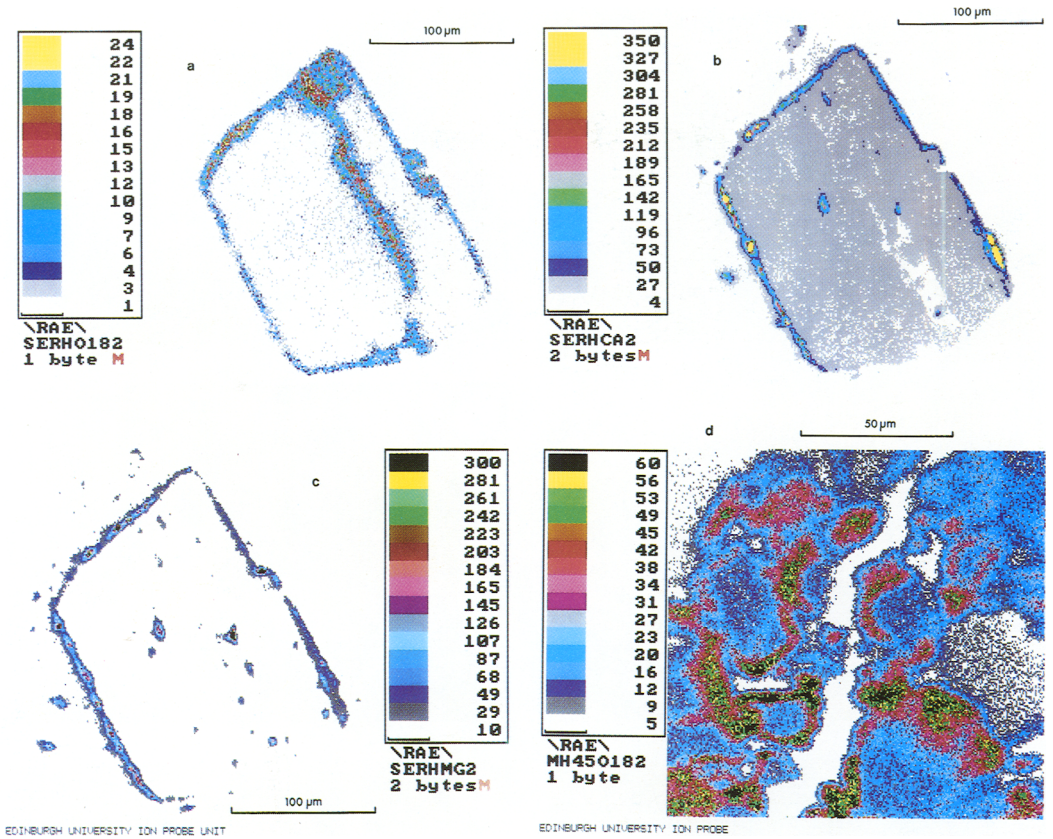

PLATE 3. (*a*) RAE image of distribution of ^{18}O in a crystal in a grain mount of Amelia albite heated for 52 hours at 17 kbars, 700 °C in $CaC^{18}O_3$. The image shows the penetration of ^{18}O along fractures open at high pressure, and into the grain edges by volume diffusion. Note that high ^{18}O areas in 3(*a*) do not correspond with high mass-40 areas in Plate 3(*b*).

(*b*) RAE image of the distribution of mass 40 in the same crystal as in 3(*a*). Note the concentration around crystal edges, where the mounting medium meets the grain, but absence of mass 40 signal from the core of the crystal. This mismatch of masses 18 and 40 demonstrates the absence of $CaC^{18}O_3$ in the grain mount.

(*c*) RAE image of the distribution of mass 24 in the same crystal as Plates 3(*a*) and (*b*). Note the concentration around the crystal edges and the correspondence with the high mass-40 areas in Plate 3(*b*).

(*d*) Scanning ion image of ^{18}O distribution in calcite-forsterite run product crystallised at 1 kbar, 650 °C for 15 minutes, with 5 wt.% H_2O–CO_2 fluid ($X(CO_2) = 0.5$) with 14% total oxygen present in the fluid as ^{18}O. Scale bar shows accumulated counts per pixel. Compare with Fig. 3.